A Computationally Assisted Approach for Designing Wearable Biosensors toward Non-invasive Personalized Molecular Analysis

Daniel Mukasa,[1,2] Minqiang Wang,[1,2] Jihong Min,[1] Yiran Yang,[1] Samuel A. Solomon,[1] Hong Han,[1] Cui Ye,[1] Wei Gao[1]*

[1]Andrew and Peggy Cherng Department of Medical Engineering, Division of Engineering and Applied Science, California Institute of Technology; Pasadena, California, 91125, USA.

[2]These authors contributed equally to this work.

*Email: weigao@caltech.edu

Wearable sweat sensors have the potential to revolutionize precision medicine as they can non-invasively collect molecular information closely associated with an individual's health status. However, the majority of clinically relevant biomarkers cannot be continuously detected in situ using existing wearable approaches. Molecularly imprinted polymers (MIPs) are a promising candidate to address this challenge but haven't yet gained widespread use due to their complex design and optimization process yielding variable selectivity. Here we introduce QuantumDock, an automated computational framework for universal MIP development toward wearable applications. QuantumDock utilizes density functional theory to probe molecular interactions between monomers and the target/interferent molecules to optimize selectivity, a fundamentally limiting factor for MIP development toward wearable sensing. A molecular docking approach is employed to explore a wide range of known and unknown monomers, and to identify the optimal monomer/crosslinker choice for subsequent MIP fabrication. Using an essential amino acid phenylalanine as the exemplar, we performed successful experimental validation of QuantumDock using solution-synthesized MIP nanoparticles coupled with ultraviolet–visible spectroscopy. Moreover, we designed a QuantumDock-optimized graphene-based wearable device that can perform autonomous sweat induction, sampling, and sensing. We, for the first time, demonstrate wearable non-invasive phenylalanine monitoring in human subjects toward personalized healthcare applications.

1. Introduction

Wearable sensors have great potential to revolutionize the field of personalized medicine as they can continuously and non-invasively monitor an individual's physiological and health status.[1–9] While commercially available wearable health monitors mainly track physical vital signs, wearable sweat biosensors could offer rich health information at molecular levels.[10–23] Continuous analysis of sweat biomarkers including amino acids, vitamins, metabolites, drugs, hormones, and proteins could have a profound impact in remote monitoring and management of a variety of health conditions such as stress, gout, metabolic disorders, cardiovascular diseases, and cancers.[24–40,21] Most currently reported wearable electrochemical sweat biosensors can only monitor a limited group of small molecules (e.g., glucose, lactate, and ions) using enzymatic or ion-selective sensors.[24–30] The majority of clinically relevant biomarkers in sweat cannot be detected in situ using these wearable sensing approaches. Bioaffinity sensors based on bioreceptors such as antibodies can be highly sensitive and selective, but are limited to single-point use and usually require additional sample preparation or washing steps.[41–44]

Molecularly imprinted polymers (MIPs) are synthetic bioreceptors fabricated via the polymerization of functional monomers in the presence of the target analyte.[45,46] Subsequent elution of the template molecule from the polymer matrix leaves target analyte-shaped imprints that can act as artificial antibodies to facilitate selective target rebinding. The integration of an additional redox probe in the sensor design can transduce such rebinding recognition into measurable electrochemical signals.[35,47] We recently demonstrated continuous monitoring of circulating metabolites and nutrients such as branched-chain amino acids in human sweat by combing MIPs with mass-producible laser-engraved graphene (LEG).[35] Despite the great promise of using MIPs in wearable sweat biosensing, MIPs have not yet gained widespread use in the field of biosensors due to their complex design and optimization process.[48] The choice of functional monomers and crosslinkers dramatically influences sensor selectivity and overall performance, rendering many MIPs ineffective for biofluid analysis due to the lack of selectivity. Considering the large library of monomer and target biomarker choices, experimental optimization of new MIPs is extremely time-consuming, costly, and substantially impedes the broad application of MIP-based wearable sensor in personalized healthcare.

Computational approaches such as semiempirical calculations and density functional theory (DFT) have great potential to simplify and accelerate the MIP design process. Although fast,

semiempirical methods utilize the neglect of diatomic differential overlap approximation which is known to significantly underestimate binding affinities, limiting the ability to correlate to experimental results. DFT enables researchers to utilize highly accurate quantum mechanics simulations to probe molecular interactions between a potential monomer and biomarker. Traditionally DFT has been used to calculate binding energies between monomers and target biomolecules, since maximizing this quantity maximizes the amount of target molecules to be absorbed which in return maximizes MIP sensitivity[49–51]. However, finding the most stable binding configuration between two biomolecules tends to be a time intensive task, further slowing down the MIP design process. Further, previous studies lack experimental validation for biomarker analysis and have not fully addressed the fundamentally limiting factor in MIP performance for in situ wearable sensing applications – selectivity.

In this work, we introduce QuantumDock, an automated computational framework for universal MIP development toward a wide range of wearable biosensing applications (**Fig. 1a**). QuantumDock utilizes quantum theory, specifically DFT, to probe molecular interactions between monomers and the target/interference molecules. QuantumDock employs a novel theory to optimize selectivity: A molecular docking approach is employed to find the most stable binding geometries and to calculate a novel selectivity metric for the optimal choice of monomer (and crosslinker when necessary), enabling accelerated MIP fabrication (**Fig. 1b–g, Supplementary Fig. 1**, and **Supplementary Video 1**). Through these innovations, QuantumDock addresses all previously discussed shortcomings of semiempirical calculations and traditional DFT and is the first standardized method for calculating binding energies reproducibly with a modern level of theory (**Supplementary Table 1**). In addition to optimizing the choice of existing monomers, QuantumDock also has the potential to explore various unknown monomers/molecules for general MIP design with potentially higher selectivities than traditionally used monomers. Using an essential amino acid phenylalanine (Phe) as the exemplar, we experimentally validated the model using solution-synthesized MIP nanoparticles (NPs) and demonstrated for the first time – the correct prediction of the exponential relation between binding energy difference and selectivity in MIPs. This is particularly important for wearable sensor field as for practical in situ body fluid analysis, selectivity is the main limiting factors of the MIP design. Moreover, we designed a skin-interfaced wearable sweat sensing system and demonstrated the potential usage of a

QuantumDock-optimized MIP wearable sensor for personalized nutritional and healthcare applications (**Fig. 1h,i**).

2. Results and discussions

2.1 The process of QuantumDock-based MIP development

Chemically selective interactions are observed naturally in antibodies, proteins, and alike. The physical basis of this phenomena has been characterized extensively, particularly with selective isotope binding. Simply put, selective binding occurs when a target molecule (Tar) binds stronger to a candidate material than an interferant molecule (Int) in their respective ground states. The strength of binding is quantified via the binding energy (E), hence selective binding is encapsulated by the inequality $E_{Tar} > E_{Int}$ or $\Delta E = E_{Tar} - E_{Int} > 0$ (**Supplementary Note 1**). For systems of molecular biomarkers, the ground state geometric configuration can be quite elusive to find. Biomolecules have multiple sites in which non-covalent interactions including hydrogen bonds, ionic bonds, and van der Waals interactions can take place (**Supplementary Figs. 2 and 3**). Finding the ground state, or the most stable interaction, between a target molecule and monomer can take a long time especially when the number of monomers and targets is very large (**Fig. 1b**). Failing to do an exhaustive search for the ground state however can yield inaccurate selectivity predictions.

To approach this issue QuantumDock employs an exhaustive yet computationally efficient docking approach in which a monomer is docked to a potential binding site on a target molecule until all binding sites have been probed (**Fig. 1c**). All noncovalent interactions that can occur in a pre-polymerized MIP solution (hydrogen bond, electrostatic, and van der Waals) are considered in this step. The energy near every binding site is quickly calculated over hundreds of potential molecular orientations using a fast-screening method, enabling an exhaustive search of the potential energy surface for its strongest binding sites (**Fig. 1d,e**). The most stable geometric conformations from this screening step are used in a final DFT calculation to determine the true ground state energies and binding selectivities (**Fig. 1f**). This process can be repeated across all targets and monomers in a computational library until the optimal choices are found (**Fig. 1g**). It should be clarified that the main application of QuantumDock is not to discover new monomers never reported before, but rather is to identify the most suitable monomer/crosslinker choices (over many monomers that could be used to prepare a biomarker MIP) with highest selectivity

performance over the many potential interferences (particularly those with similar molecular structures) in their specific biosensing applications. The QuantumDock-based MIP optimization can serve as a universal approach for designing next-generation wearable biosensors that can monitor a broad spectrum of biomarkers related to various health conditions.

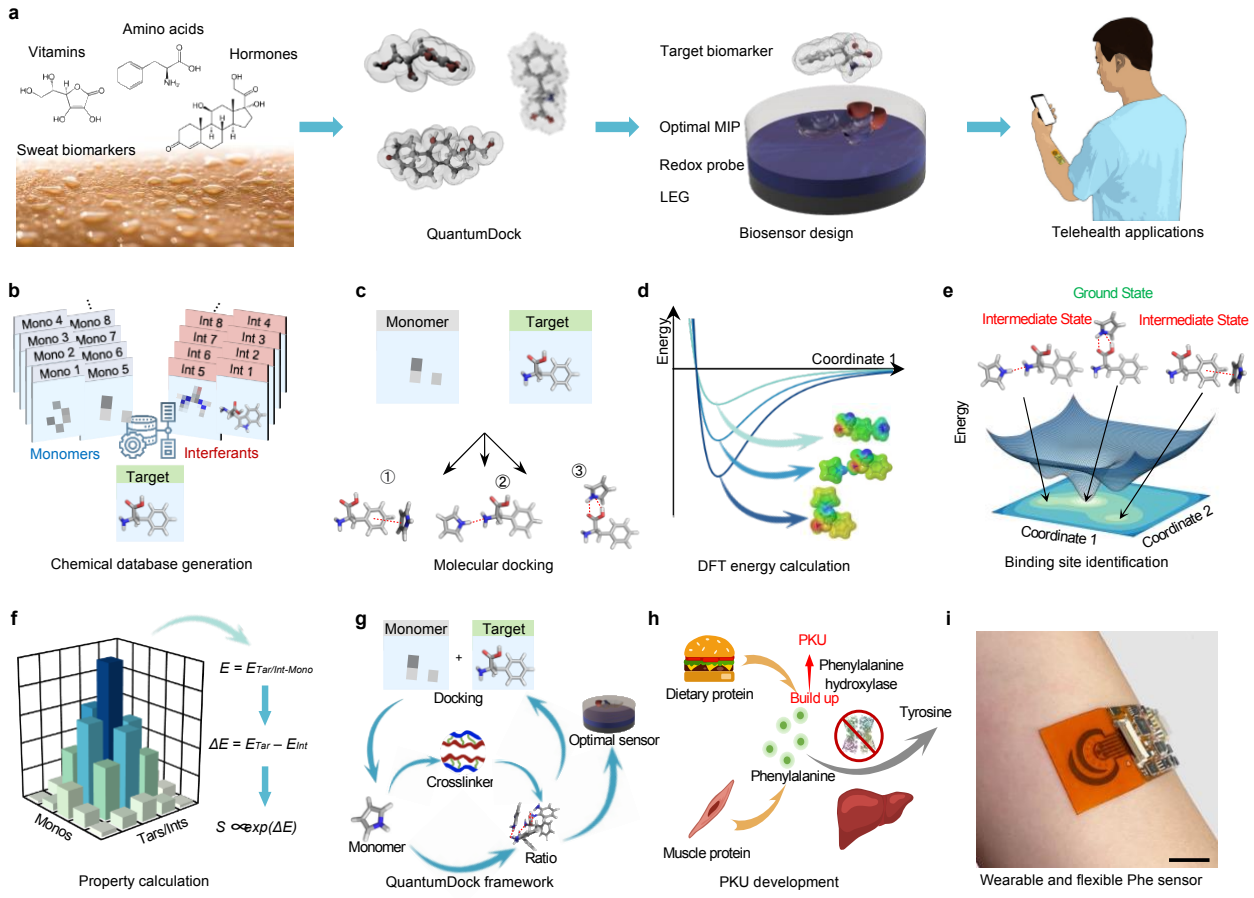

Figure 1. QuantumDock, a rational bioaffinity biosensor design approach for wearable molecular monitoring. a, QuantumDock-enabled molecularly imprinted polymer (MIP)-based wearable biosensor design and optimization for circulating biomarker monitoring toward personalized healthcare. LEG, laser-engraved graphene. **b–g**, The general procedures of QuantumDock-based MIP design: chemical database generation (**b**), molecular docking (**c**), density functional theory (DFT)-based binding energy calculation (**d**), binding site and ground state identification (**e**), target/interference-monomer property calculation for selectivity evaluation (**f**), repeated computational optimization across targets and monomers libraries (**g**). E, binding energy; Tar, target; Int, interferent; Mono, monomer; S, selectivity. **h**, The role of phenylalanine (Phe) in phenylketonuria (PKU) development. **i**, A fully-integrated wearable sensor based on

QuantumDock-enabled Phe MIP for wireless Phe sensing toward PKU and nutritional monitoring. Scale bar, 1 cm.

2.2 Quantum Dock-enabled computational Phe MIP optimization

Being an essential amino acid, Phe plays an important role in the production of tyrosine and multiple crucial neurotransmitters (e.g., dopamine, norepinephrine, and epinephrine).[52] It is also a well-known biomarker for phenylketonuria (PKU), an inherited disorder in which the human body is unable to process Phe to tyrosine, causing an array of bodily harm.[53,54] Despite the importance and urgent demand of personalized Phe monitoring, its wearable sensing in human subjects *via* sweat analysis has not been demonstrated. As such we chose Phe as a model biomarker for MIP development. Using the QuantumDock procedure, we docked 7 commonly used monomers to Phe including pyrrole (PYR), 4-vinmylbenzoic acid (4VB), acrylamide (ACM), methacrylic acid (MAA), aniline (ANI), 3-aminophenylboronic acid (APB), and o-phenylenediamine (OPD) for MIP fabrication (**Fig. 2a**). Although many of the monomers we chose here could be used to prepare the Phe MIP based on past reports, there is no study on comparing the selectivity performance of these monomers over the major interferences (particularly those with similar molecular structures). Potential binding orientations between Phe and each monomer were first screened using semiempirical quantum mechanical calculations (**Fig. 2b**). Such methods are particularly advantageous as they allow for quick yet fairly accurate approximations of binding energies in monomer-biomarker complexes, taking on the order of seconds to calculate molecular energies. Results from this screening correctly revealed two potential binding sites on Phe on the carboxyl (COOH) and amine (NH_2) functional groups. Semiempirical calculations are however historically known to have less accuracy than more intricate DFT calculations for calculating binding energies as they compromise accuracy for speed[55,56]. This inaccuracy could lead to downstream errors where the predicted sensitivities and selectivities would be poorly ranked, emphasizing the need for more accurate DFT energy calculations (**Supplementary Fig. 4**). Subsequent DFT energy calculations on the most stable screened molecules indicate that the carboxylic group on Phe tends to form the most stable bonds with all monomers in our study (**Fig. 2c, d** and **Supplementary Fig. 3**). This is because Phe is highly charged and has both a hydrogen bond donor and acceptor making a relatively stronger and larger binding site for strong hydrogen bonds, in agreement with molecularly electrostatic potential calculation (**Fig. 2e**).

The ground state binding energy, being the most stable or most negative calculated energy, is stored from these DFT calculations (**Fig. 2f** and **Supplementary Fig. 5**). Following this quantum dock method, we find these final ground state energies to be highly reproducible (**Supplementary Fig. 6**). Traditionally the ground state binding energy has been used to optimize MIP sensitivity, with higher binding energies indicating a MIP will bind more target molecules to its surface. This subsequently aids detection of low concentrations when less target molecules are present in solution. Despite the use of this metric in theory, there is not much variation amongst our calculated binding energies. Of the 7 monomers used in this study, 5 (APB, ACM, OPD, MAA, VB4) had binding energies to Phe within the top quartile of calculated energies, indicating relatively low variance from monomer to monomer. Therefore, only using a high binding energy as a metric for monomer choice in MIP fabrication does not significantly slim our number of monomer choices. We therefore turn to evaluating theoretically calculated selectivity's to make greater distinction between molecules. Since selectivity (S) can be calculated as $S \propto exp(\Delta E/(k_B T))$, where k_B and T are Boltzmann constant and temperature respectively (**Supplementary Note 1**), we calculate the binding energy difference ΔE between monomer/target and monomer/interferent as a metric to rank our monomer selection. Selectivity calculations indicate that clearly OPD, MAA, and 4VB on average have the highest potential of being selective against multiple interferants with a similar chemical structure to Phe including tyrosine (Tyr), valine (Val), leucine (Leu), isoleucine (Ile), and dopamine (DA) (**Fig. 2g**). Such results also confirm that even though monomer PRY was also used in literature to prepare Phe MIP, the PYR MIPs suffer from bad selectivity against most chemically similar molecules. By evaluating 5 less commonly used monomers which include 1,2-ethanediol (12E), acrylic acid (ACA), phenol (PHN), 2-vinylpyridine (2VP), 2-aminophenol (2AM), we demonstrate that multiple new monomers perform better selectivity for Phe against chemically similar molecules (i.e., three other amino acid: Leu, Ile, and Val) than multiple more commonly used monomers (e.g., PYR and APB) (**Supplementary Figs. 7** and **8**), indicating the powerful capability of the QuantumDock for exploring new MIP design. It should be also noted that QuantumDock is fully capable of exploring unknown monomers along with those that have been previously reported. To demonstrate this, we have simulated two further classes of unknown monomers that can be used in MIP fabrication (**Supplementary Figs. 7–9**): The first being 3 monomers (methacrylamide, vinyl acetate, and 1-vinylimidazole) that have never been used to make a MIP; The second set of molecules are generated using Generative Examination Networks

(GEN)[57], a popular generative adversarial neural network capable of generating simplified molecular input line entry system (SMILES) strings (text based encodings of molecules)[58]. QuantumDock can interpret these novel SMILES strings, generate their 3D conformations, and test their selectivity against our previously listed interferants. The combination of a generative algorithm with QuantumDock shows the algorithms full potential of being able to generate, and screen through countless monomers for MIP development. Screening through a larger number of monomers opens up the possibility of finding novel monomers with higher selectivity and sensitivity. Interestingly enough, the novel topology of molecules generated *via* the GEN neural network show much higher selectivities than the typical monomers used in MIP fabrication (**Supplementary Figs. 8** and **9**).

Furthermore, calculations in which the monomer template ratio was modified showed a much more efficient means of increasing both monomer template binding energies and binding energy differences (**Fig. 2h,i**). Increasing the number of monomers in the monomer template ratio allowed more binding sites on the Phe template to be accessed, increasing the binding energy and binding energy difference of the target-monomer complex. This increase seems to have diminishing returns once binding sites become saturated, the binding energy of the target-monomer complex stops increasing as rapidly. Finally, we calculate the binding energies between Phe and various potential crosslinkers for use of study (**Fig. 2j**). It is well established that crosslinkers with low binding energies to the target molecule have the best potential for MIP fabrication.[59] Crosslinkers which bind poorly to the target molecule are less likely to nonspecifically bind to it in the polymerization process, and in effect more likely to contribute to the rigidity of the final polymer structure as intended. We therefore chose divenylbenze (DVB) as our crosslinker of choice. Its low binding energy to Phe can be attributed to it not having any hydrogen bond donor or acceptor atoms, making it an optimal candidate.

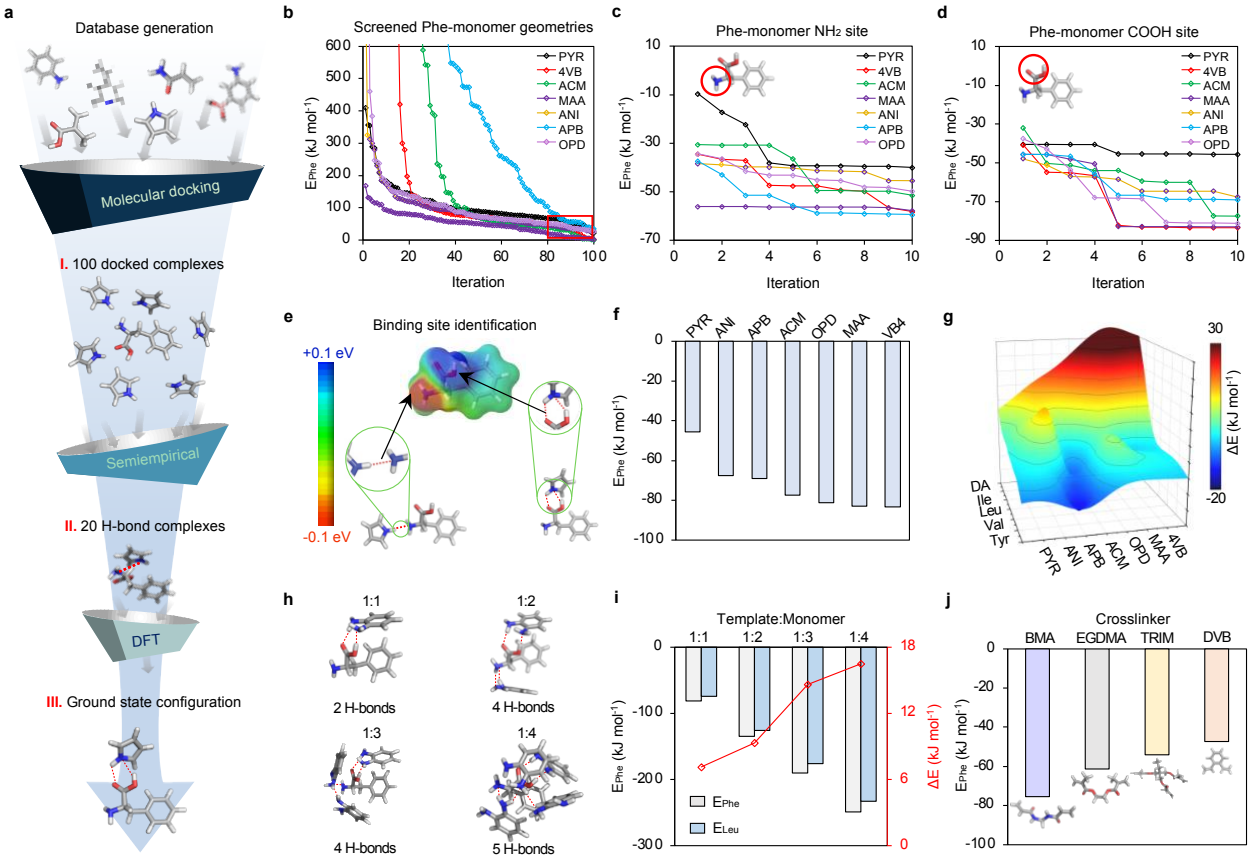

Figure 2. QuantumDock-based computational Phe MIP optimization. a, The procedure of QuantumDock-based Phe-monomer ground state configuration. H-bond, hydrogen bond. **b**, Semiempirical energy calculations based on 100 docked monomer-Phe complexes for each monomer. PYR, pyrrole; 4-VB, 4-vinmylbenzoic acid; ACM, acrylamide; MAA, methacrylic acid; ANI, aniline; APB, 3-aminophenylboronic acid; OPD, o-phenylenediamine. **c**,**d**, DFT energy calculations on the most stable screened molecules based on Phe-monomer NH_2 site (**c**) and Phe-monomer COOH site (**d**). **e**, Electrostatic potential of a Phe molecule. **f**, DFT-calculated binding energy of Phe-monomer. **g**, Colored mapping of the binding energy differences between Phe-monomer and interference-monomer complexes. Tyr, tyrosine; Val, valine; Leu, leucine; Ile, isoleucine; DA, dopamine. **h**, H-bonds formed in Phe-OPD complexes (ratio 1:1, 1:2, 1:3, and 1:4). **i**, Binding energies of Phe/OPD and Leu/OPD (target versus monomer ratio 1:1, 1:2, 1:3, and 1:4), and corresponding bonding energy differences. **j**, Binding energies of Phe/crosslinker. BMA, butyl methacrylate; EGDMA, ethylene glycol dimethylacrylate; TRIM, trimethylolpropane trimethacrylate; DVB, divinylbenzene.

2.3 Experimental validation of QuantumDock using solution-synthesized MIP NPs

To experimentally validate the QuantumDock-based computationally optimized MIP, a series of MIP NPs were synthesized and characterized by the binding/adsorption amount toward target and interferent molecules. All MIP NPs were prepared in a solution containing Phe, monomer and crosslinker molecules of choice under 60 ºC with azobisisobutyronitrile as the initiator (**Fig. 3a**). Methanol was added into water (4:1 (v/v)) as a solvent to maximize the binding energy (**Supplementary Fig. 10**). Non-imprinted polymer nanoparticles (NIP NPs) were fabricated following the same procedure with the exclusion of the Phe template molecule. The resultant MIP NPs have a size of ~50 nm according to the scanning electron microscopy (SEM) image (**Fig. 3b**). Energy dispersive X-ray (EDX) analysis of the MIP NPs before and after target extraction showed a sharp decrease at the carbon alpha emission lines after Phe extraction (**Fig. 3c**), suggesting the successful extraction of Phe molecules. Such target extraction was further validated by conducting ultraviolet–visible spectroscopy (UV-Vis) before and after extraction on a sample containing MIP NPs. The absorbance peak at ~270 nm wavelength was consistent with Phe's UV-absorption maxima decreases after target extraction (**Fig. 3d**). It should be noted that the peak is however still present as there will be some Phe molecules trapped inside the polymer matrix after extraction.

Isotherm experiments were conducted to investigate the binding dynamics of Phe to various MIP NPs fabricated with different monomers. A linear relationship was identified between the absorbance peak height at around ~270 nm and the Phe concentration in the range between 500 µM and 20 mM (**Fig. 3e**). The maximal absorption of each MIP NPs Q_e was calculated as $Q_e = (C_0-C_t)/(m/V)$ where m/V is the MIP NP density, C_0 is the initial target molecule solution concentration, and C_t is the concentration recorded after incubating MIP NPs in solution. An incubation time of at least 6 minutes was determined to be optimal as Q_e tended to maximize at this time, indicating the system had reached thermodynamic equilibrium (**Fig 3f**). Q_e results show a distinction between each monomer with MAA being highest on average and PYR the lowest next to its NIP counterpart (**Fig. 3g**). These results are in agreement with the DFT calculations of the binding energy between monomers and Phe (**Fig. 3h**), indicating that when a target molecule binds stronger to a MIP binding site, more of said target molecules will bind to the MIP. This effect can be used to increase the MIP's sensitivity by binding more of the target even at low concentrations, hence increasing the resulting sensor signal response. Further, we have successfully validated that crosslinkers with low binding energy to template molecules lead to higher Q_e (**Fig. 3i**).

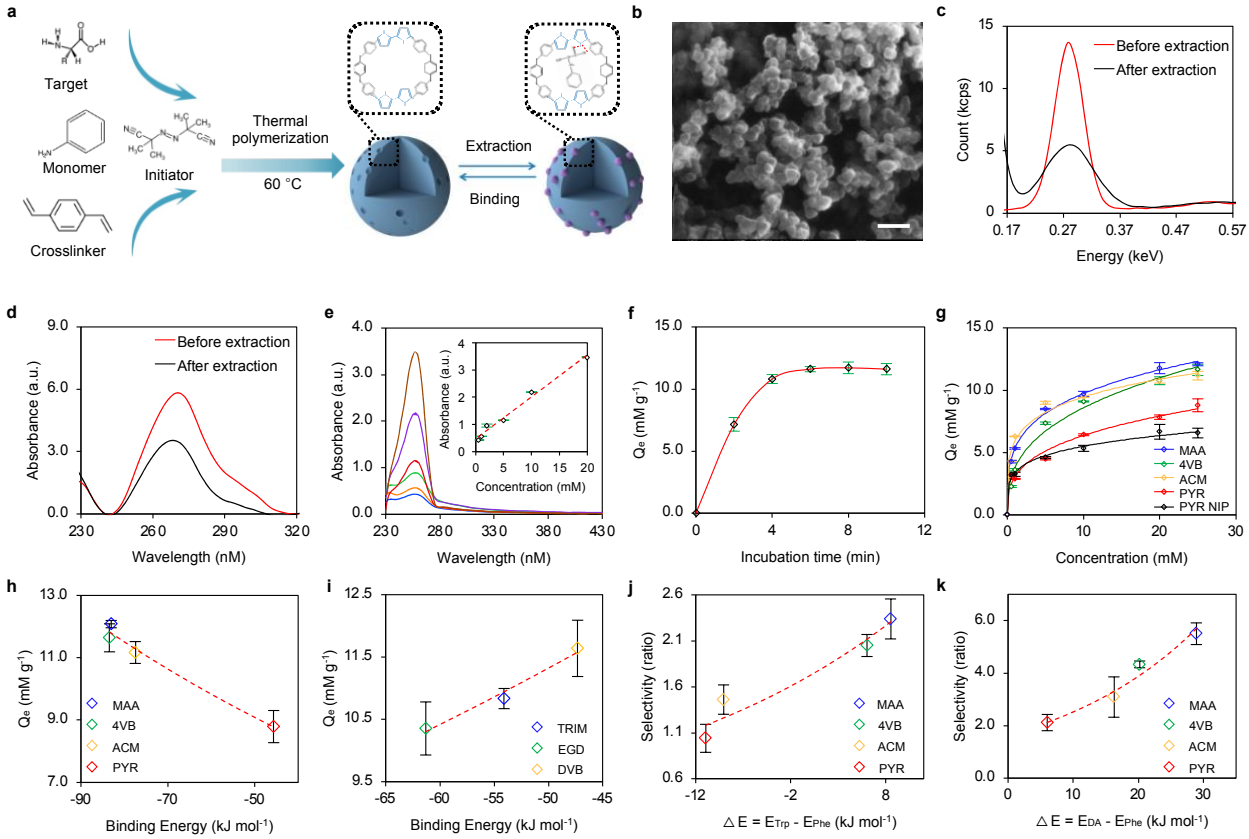

Figure 3. Experimental validation of QuantumDock-optimized Phe MIP using solution-synthesized NPs. a, Solution synthesis process of Phe MIP NPs. **b**, Scanning electron microscopy (SEM) image of Phe-PYR MIP NPs. Scale bar, 200 nm. **c**, Energy-dispersive X-ray spectroscopy results of carbon elements in the Phe-PYR MIP NPs before and after target extraction. **d**, Ultraviolet–visible spectroscopy (UV-Vis) absorbance of Phe-PYR MIP NPs before and after template extraction. **e**, UV-Vis absorbance of Phe-PYR MIP NPs after incubation of 500 µM–20 mM Phe. Insets, calibration plots with a linear fit. **f**, The maximum adsorption amount (Q_e) of Phe-PYR MIP NPs over incubation time. **g**, Q_e of Phe/monomer MIP NPs upon incubation in 500 µM–20 mM Phe. **h**, The relationship between Q_e of the Phe MIP NPs and calculated Phe-monomer binding energies. **i**, The relationship between Q_e of the Phe MIP NPs and calculated Phe-crosslinker binding energies. **j,k**, Selectivity of Phe MIP NPs based on different monomers over interferents DA (**j**) and Trp (**k**). All error bars represent the s.d. from three measurements.

Further studies were carried out to probe the MIPs capability to selectively bind to Phe over other interfering molecules. Selectivity $S = Q_e^{Tar}/Q_e^{Int}$ is measured as the amount of target molecules a MIP particle can absorb (Q_e^{Tar}) divided by the amount of interferant molecules the MIP is capable

of absorbing (Q_e^{Int}). This selectivity metric directly indicates a MIPs capability to preferentially bind its imprinted target molecule over any potentially coexisting interferant. To our knowledge no such study has probed into the correlation using this measured selectivity nor any theoretical description of selectivity. As illustrated in **Fig. 3j,k**, using DA and Trp as the exemplar interferents (**Supplementary Fig. 11**), our selectivity results of the Phe MIP NPs verified the previously described theoretical derivation of selectivity which states that selectivity is exponentially proportional to the binding energy difference. This result is especially interesting as it shows optimizing selectivity computational can quickly yield significant improvements in a MIPs selectivity, hence drastically increasing a biosensors performance. It should be noted that the binding energy difference calculated by the intermediate binding states could lead to large prediction error (**Supplementary Fig. 12**). Therefore, QuantumDock's capability to reproducibly find the most stable ground state binding energies is critical for selectivity prediction.

2.4. Electrochemical graphene sensor development toward continuous sweat Phe monitoring

Applying the QuantumDock-optimized MIPs to wearable biosensors, we developed a flexible electrochemical biosensor using the Phe MIP as the bio-receptor to specifically capture free Phe molecule in the sweat (**Fig. 4a**). Considering the low concentration of Phe in human sweat (μM level), flexible laser-engraved graphene (LEG) on a polyimide substrate was chosen as the electrode material to increase the sensor sensitivity and skin conformability as it has a large surface area, high electrochemical catalytic activity, high mechanical flexibility, and can be mass-producible at a large scale (**Supplementary Figs. 13** and **14**)[33,60]. To prepare the biosensor, the Phe MIP layer was directly electro-polymerized onto an LEG electrode followed by the target extraction. The selective recognition molecule into the imprinted polymeric layer can be further converted to a measurable electrochemical signal by incorporating a redox active reporter (RAR) layer between the Phe MIP film and the LEG electrode. The target adsorption reduces the exposure of the RAR (nickel hexacyanoferrate here) to the sample matrix and further block the electron transfer and thus leads to a decreased redox signal (**Fig. 4a**). The SEM image of the Phe sensor clearly shows a highly porous 3D structure of the LEG covered uniformly by a polymeric MIP film and RAR NPs (**Fig. 4b**).

The successful MIP electrochemical sensor preparation was characterized and validated using differential pulse voltammetry (DPV) (**Fig. 4c**). The LEG-RAR displayed the highest reduction

peak of RAR which decreased substantially after polymerization of the polymer film (LEG-RAR-MIP-before) due to the RAR blockage by the polymer; the extraction of the template molecule (Phe) led to the target selective cavities and increased exposure of the RAR site to the sample matrix, resulting in an increased reduction signal (**Fig. 4c**). In addition, the MIP sensor preparation was further validated using open-circuit potential-electrochemical impedance spectroscopy (OCP-EIS): the electrode resistance in Nyquist plots decreased after the extraction of the template, suggesting the increased exposure for RAR to the sample matrix (**Fig. 4d**).

For Phe quantification, DPV was used to measure the RAR's reduction peak of the LEG-RAR-MIP Phe sensor, where the decrease in the peak current correlated with an increase in Phe concentration. A log-linear relationship between the decreased peak current density height of the DPV voltammograms and Phe concentration (**Fig. 4e**) was achieved with a sensitivity of 353.94 nA mm^{-2} per decade of concentration, when OPD was used as the monomer. The flexible LEG sensors demonstrated stable electrochemical performance under mechanical deformation (**Fig. 4f**). Moreover, the sensor showed excellent selectivity toward other analytes with similar structures such as Leu: a substantially higher DPV reduction peak decrease was observed for Phe detection compared to that obtained after incubation with interferent Leu (**Fig. 4g**). Overall, compared with APB and PYR MIP-based sensors, the OPD MIP-based sensors show improved selectivity for the detection of Phe over common physiological-level interferents (**Fig. 4h** and **Supplementary Fig. 15**), consistent with the QuantumDock's computational results on ΔE (**Fig. 2g**).

To enable automatic Phe detection in human sweat toward non-invasive wearable sensing, we utilized here an in-situ calibration strategy involving two-step DPV scans: the first scan was performed to determine the background signal before target recognition while the second scan was performed after incubation to determine the reduction signal change; in-situ regeneration was realized by applying constant current to the MIP electrode to repel the bound Phe molecules (**Fig 4i**). Continuous and repetitive Phe detection between low concentration and high concentration can thus be realized automatically (**Fig 4j**). Considering that the variations of individual's sweat composition could affect the in situ Phe measurement, we characterized the dependence of pH or solution conductivity (Na^+) on the response of the Phe sensor, as illustrated in **Fig 4k,l**. Considering that both pH and Na^+ have substantial influence on the Phe sensor reading, it is important to simultaneously monitor pH and Na^+ levels for in situ accurate sweat analysis.

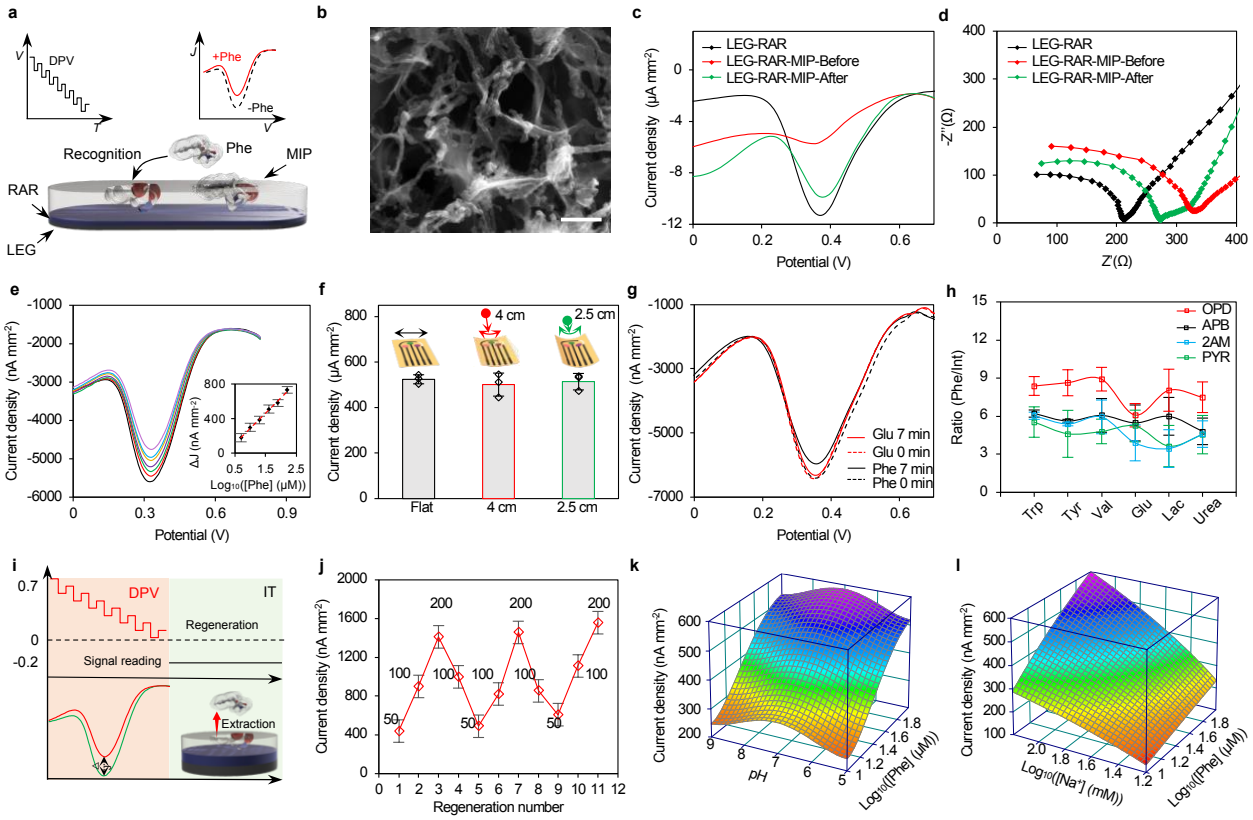

Figure 4. Characterization of electrochemical graphene-based Phe sensor. a, The mechanism of the electrochemical Phe MIP sensor based on the laser-engraved graphene (LEG) and the redox-active reporter (RAR). **b**, SEM image of an LEG-RAR-MIP electrode. Scale bar, 1 μm. **c**,**d**, Differential pulse voltammetry (DPV) (**c**) and electrochemical impedance spectroscopy (EIS) (**d**) results of an LEG-RAR electrode, an LEG-RAR-MIP electrode before target extraction, and an LEG-RAR-MIP electrode after target extraction. Z, impedance; Z', resistance; Z'', reactance. **e**, DPV voltammograms and the corresponding calibration curves of Phe detection using the LEG-RAR-MIP sensors. **f**, DPV peak height of current density of the Phe sensor under mechanical deformation. Error bars represent the s.d. from three sensors. **g**, DPV voltammograms of an LEG-RAR-MIP Phe sensor before and after incubation in Phe and Leu. **h**, The target (Phe) to interference signal ratios of the LEG-RAR-OPD, LEG-RAR-APB, and LEG-RAR-PRY MIP sensors. **i**, Calibration strategies of the wearable LEG-MIP sensors involving a two-step DPV-scan calibration for automatic in situ Phe analysis. **j**, In situ continuous sensing and regeneration of an LEG–RAR–MIP Phe sensor in Phe solutions. **k**,**l**, Color maps showing the dependence of the LEG-RAR-MIP Phe sensor response on pH (**k**) and Na^+ (**l**) concentrations. All error bars represent the s.d. from three sensors.

2.5 Development of the fully-integrated wearable and flexible Phe sensor patch

To enable the continuous Phe monitoring, a wireless wearable sensor patch was developed based on our previously established platform[33] that contains two carbachol-loaded LEG iontophoresis electrodes for prolonged localized on-demand sweat induction, a laser-engraved microfluidic module for sweat sampling, and a sensor array consisting of a QuantumDock-optimized LEG-OPD MIP Phe sensor (**Fig. 5a–c** and **Supplementary Fig. 16**). The integrated system can perform on-demand iontophoresis, multimodal electrochemical sensing, and wireless communication (**Fig. 5d** and **Supplementary Fig. 17**). Electrochemical ion-selective pH and Na^+ sensors are intergraded into the wearable sensor patch to realize accurate wearable Phe analysis in sweat monitoring via real-time sensor calibration in real time (**Fig. 5e,f**). The accuracy of the wearable Phe sensor patch for analyzing raw human sweat was verified using the gold standard gas chromatography-mass spectrometry (GC-MS): a very high correlation between the results from sensors and from GC-MS was observed (**Fig. 5g**). The sensor patch is able to autonomously induce sweat through iontophoresis (to deliver carbachol below the skin) at rest without the need for vigorous exercise; a microfluidic module was used to efficiently sample the fresh sweat generated from the sweat gland due to the nicotinic effects of carbachol to facilitate the real-time sweat analysis (**Fig. 5h, Supplementary Fig. 18**, and **Supplementary Video 2**).

Clinical on-body evaluation of the wearable system toward personalized nutritional monitoring was performed via sensing of sweat Phe in human subjects at rest with and without Phe supplement intake. The DPV signal from the Phe sensor worn on the subjects' wrist was wirelessly transmitted along with temperature, pH and Na^+ sensor readings to the interface that automatically performed calibration for the accurate quantification of sweat Phe (**Fig. 5i–l**, **Supplementary Fig. 19**, and **Supplementary Video 3**). As expected, rapidly rising Phe levels in sweat were observed from all two subjects after Phe supplement intake while the Phe levels remained stable during the fasting studies. This represents the first demonstration of continuous non-invasive wearable sweat Phe sensing in human subjects. Such a good capability indicates the great potential for non-invasive Phe monitoring using the wearable sensor and opens the door for PKU management through personalized sensor-guided dietary intervention.

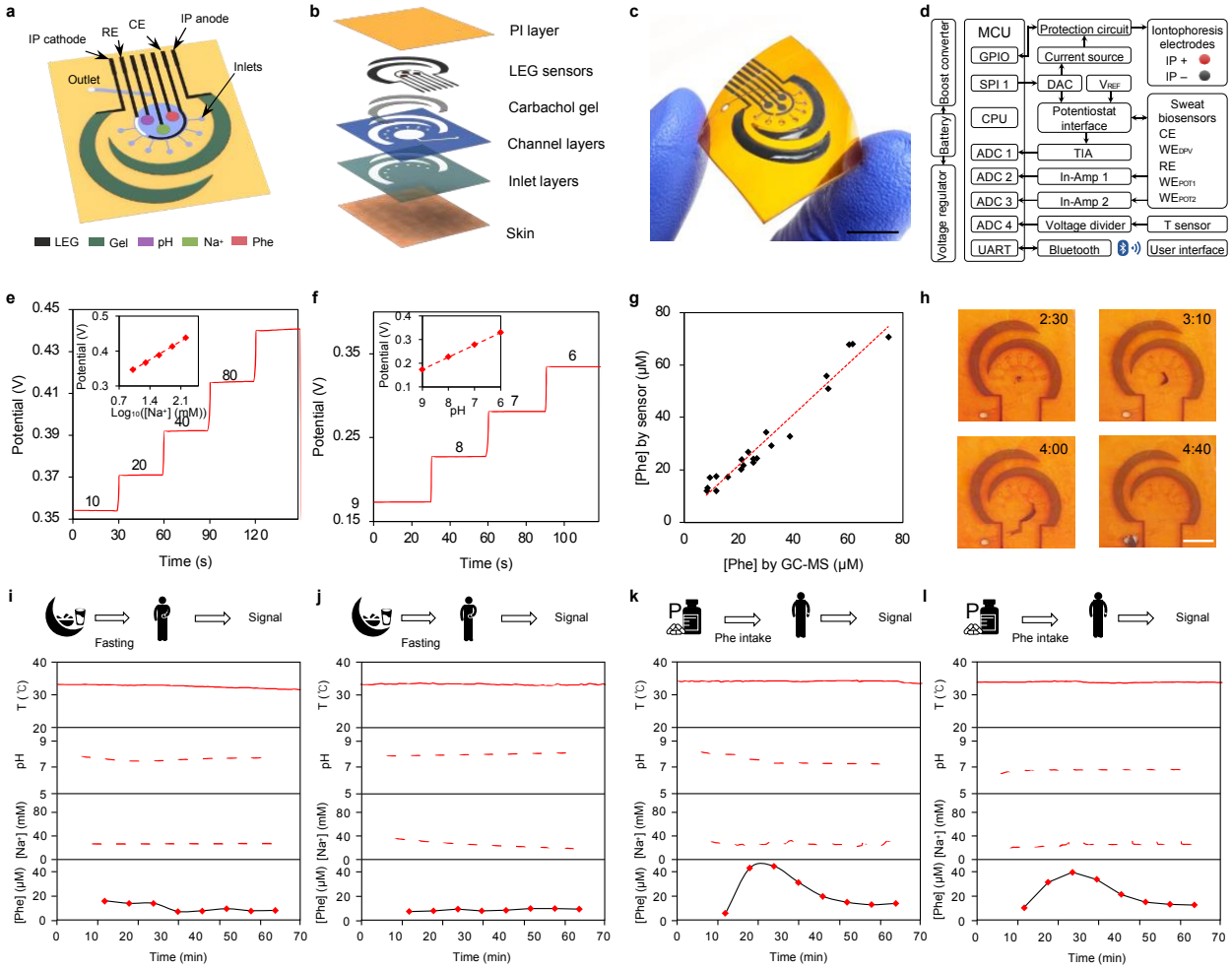

Figure 5. Design and in vivo evaluation of the fully-integrated wearable flexible MIP-based Phe sensor. a,**b**, Schematic (**a**) and layer assembly (**b**) of the wearable microfluidic Phe sensor patch for autonomous sweat induction, sampling and biosensing. CE, counter electrode; RE, reference electrode; IP, iontophoresis. **d**, Block diagram of electronic system of the wearable Phe sensor. CPU, central processing unit; POT, potentiometry; In-Amp, instrumentation amplifier; MCU, microcontroller; TIA, trans-impedance amplifier; WE, working electrode. **e**,**f**, Calibration plots obtained using the wearable system from the Na^+ (**e**) and pH (**f**) sensors. **g**, Validation of Phe sensors for raw sweat samples (n = 21) analysis against gas chromatography–mass spectrometry (GC-MS). **h**, On-body evaluation of the microfluidic patch for efficient sweat induction and sampling at rest. Timestamps represent the period (min) after a 5-min iontophoresis session. Black dye was used in the reservoir to facilitate the direct visualization of sweat flow in the microfluidics. Scale bar, 5 mm. **i**,**j**, Autonomous Phe monitoring of two healthy subjects using the wearable sensors at a fasting state. **k**,**l**, Autonomous Phe monitoring of two healthy subjects using the

wearable sensors after Phe intake. For **i–l**, a 5-minute iontophoresis was performed in the beginning of the trial followed by multiplexed data recording. Temperature, pH, Na^+ was recorded simultaneously for signal calibration.

3. Conclusion

We demonstrated a computational framework – QuantumDock – for optimizing MIP performance toward a wide range of wearable biosensing applications. Through DFT-based probing of intermolecular interactions between monomers and the targets/interferents, we were able to develop MIP-based sensors with enhanced selectivity, a crucial factor for in situ wearable biomarker analysis. Through the screening a number of molecules, we demonstrated that QuantumDock also has the potential to explore a wide range of commonly used and unknown monomers for designing better MIPs. We successfully validated the QuantumDock-based MIP design and optimization using solution-synthesized MIP NPs. We further show the potential for generative artificial intelligence in materials design by using GEN to generate novel monomers with significantly higher theoretical selectivities than commonly used MIP monomers. Based on the QuantumDock-optimized MIP, we also developed a laser-engraved graphene-based wearable electrochemical Phe sensor capable of autonomous sweat extraction, sampling, and sensing without the need for vigorous exercise. The first wearable non-invasive Phe monitoring in human subjects revealed the high potential of such technology for personalized nutritional and healthcare applications. As QuantumDock is a universal sensor optimization approach that can be easily adapted toward other important biomarkers in human body fluids, we envision that it will enable the demonstration of high-performance MIP sensors for the analysis of a wide range of biomarker and facilitate the realization of practical wearable healthcare applications.

Supporting Information

Supporting Information is available from the Wiley Online Library or from the author.

Acknowledgements

This work was funded by the National Science Foundation grant 2145802, National Institutes of Health grants R01HL155815 and R21DK13266, Office of Naval Research grants N00014-21-1-2483 and N00014-21-1-2845, and Heritage Medical Research Institute. We gratefully acknowledge critical support and infrastructure provided for this work by the Kavli Nanoscience

Institute at Caltech and thank Dr. Matthew Hunt for the help. The computations presented here were conducted in the Resnick High Performance Computing Center, a facility supported by Resnick Sustainability Institute at the California Institute of Technology. We are also thankful for the support from Prof. William A. Goddard in the theoretical and computational implementation of QuantumDock, along with providing access to extra computing resources.

Competing interests

The authors declare no competing interests.

Data and materials availability

All data are available in the main text or the supplementary materials. Source data for human studies are provided with this paper.

Keywords

Wearable sensors, sweat, molecularly imprinted polymers, density functional theory, graphene.

References

[1] T. R. Ray, J. Choi, A. J. Bandodkar, S. Krishnan, P. Gutruf, L. Tian, R. Ghaffari, J. A. Rogers, *Chem. Rev.* **2019**, *119*, 5461.
[2] C. Xu, Y. Yang, W. Gao, *Matter* **2020**, *2*, 1414.
[3] M. L. Hammock, A. Chortos, B. C.-K. Tee, J. B.-H. Tok, Z. Bao, *Adv. Mater.* **2013**, *25*, 5997.
[4] Y. Luo, M. R. Abidian, J.-H. Ahn, D. Akinwande, A. M. Andrews, M. Antonietti, Z. Bao, M. Berggren, C. A. Berkey, C. J. Bettinger, J. Chen, P. Chen, W. Cheng, X. Cheng, S.-J. Choi, A. Chortos, C. Dagdeviren, R. H. Dauskardt, C. Di, M. D. Dickey, X. Duan, A. Facchetti, Z. Fan, Y. Fang, J. Feng, X. Feng, H. Gao, W. Gao, X. Gong, C. F. Guo, X. Guo, M. C. Hartel, Z. He, J. S. Ho, Y. Hu, Q. Huang, Y. Huang, F. Huo, M. M. Hussain, A. Javey, U. Jeong, C. Jiang, X. Jiang, J. Kang, D. Karnaushenko, A. Khademhosseini, D.-H. Kim, I.-D. Kim, D. Kireev, L. Kong, C. Lee, N.-E. Lee, P. S. Lee, T.-W. Lee, F. Li, J. Li, C. Liang, C. T. Lim, Y. Lin, D. J. Lipomi, J. Liu, K. Liu, N. Liu, R. Liu, Y. Liu, Y. Liu, Z. Liu, Z. Liu, X. J. Loh, N. Lu, Z. Lv, S. Magdassi, G. G. Malliaras, N. Matsuhisa, A. Nathan, S. Niu, J. Pan, C. Pang, Q. Pei, H. Peng, D. Qi, H. Ren, J. A. Rogers, A. Rowe, O. G. Schmidt, T. Sekitani, D.-G. Seo, G. Shen, X. Sheng, Q. Shi, T. Someya, Y. Song, E. Stavrinidou, M. Su, X. Sun, K. Takei, X.-M. Tao, B. C. K. Tee, A. V.-Y. Thean, T. Q. Trung, C. Wan, H. Wang, J. Wang, M. Wang, S. Wang, T. Wang, Z. L. Wang, P. S. Weiss, H. Wen, S. Xu, T. Xu, H. Yan, X. Yan, H. Yang, L. Yang, S. Yang, L. Yin, C. Yu, G. Yu, J. Yu, S.-H. Yu, X. Yu, E. Zamburg, H. Zhang, X. Zhang, X. Zhang, X. Zhang, Y. Zhang, Y. Zhang, S. Zhao, X. Zhao, Y. Zheng, Y.-Q. Zheng, Z. Zheng, T. Zhou, B. Zhu, M. Zhu, R. Zhu, Y. Zhu, Y. Zhu, G. Zou, X. Chen, *ACS Nano* **2023**, *17*, 211.

[5] E. Shirzaei Sani, C. Xu, C. Wang, Y. Song, J. Min, J. Tu, S. A. Solomon, J. Li, J. L. Banks, D. G. Armstrong, W. Gao, *Sci. Adv.* **2023**, *9*, eadf7388.
[6] M. Sang, K. Kang, Y. Zhang, H. Zhang, K. Kim, M. Cho, J. Shin, J. Hong, T. Kim, S. K. Lee, W. Yeo, J. W. Lee, T. Lee, B. Xu, K. J. Yu, *Adv. Mater.* **2022**, *34*, 2105865.
[7] K. Meng, X. Xiao, W. Wei, G. Chen, A. Nashalian, S. Shen, X. Xiao, J. Chen, *Adv. Mater.* **2022**, *34*, 2109357.
[8] X. Liang, M. Zhu, H. Li, J. Dou, M. Jian, K. Xia, S. Li, Y. Zhang, *Adv. Funct. Mater.* **2022**, *32*, 2200162.
[9] K. Chun, S. Seo, C. Han, *Adv. Mater.* **2022**, *34*, 2110082.
[10] Y. Yang, W. Gao, *Chem. Soc. Rev.* **2019**, *48*, 1465.
[11] J. Kim, A. S. Campbell, B. E.-F. de Ávila, J. Wang, *Nat. Biotechnol.* **2019**, *37*, 389.
[12] M. Bariya, H. Y. Y. Nyein, A. Javey, *Nat. Electron.* **2018**, *1*, 160.
[13] J. Heikenfeld, A. Jajack, B. Feldman, S. W. Granger, S. Gaitonde, G. Begtrup, B. A. Katchman, *Nat. Biotechnol.* **2019**, *37*, 407.
[14] A. J. Bandodkar, W. J. Jeang, R. Ghaffari, J. A. Rogers, *Ann. Rev. Anal. Chem.* **2019**, *12*, 1.
[15] J. R. Sempionatto, J. A. Lasalde-Ramírez, K. Mahato, J. Wang, W. Gao, *Nat. Rev. Chem.* **2022**, *6*, 899.
[16] J. Xu, Y. Fang, J. Chen, *Biosensors* **2021**, *11*, 245.
[17] H. C. Ates, P. Q. Nguyen, L. Gonzalez-Macia, E. Morales-Narváez, F. Güder, J. J. Collins, C. Dincer, *Nat. Rev. Mater.* **2022**, *7*, 887.
[18] H. Shen, H. Lei, M. Gu, S. Miao, Z. Gao, X. Sun, L. Sun, G. Chen, H. Huang, L. Chen, Z. Wen, *Adv. Funct. Mater.* **2022**, *32*, 2204525.
[19] L. Wang, J. Lu, Q. Li, L. Li, E. He, Y. Jiao, T. Ye, Y. Zhang, *Adv. Funct. Mater.* **2022**, *32*, 2200922.
[20] H. Zhao, X. Zhang, Y. Qin, Y. Xia, X. Xu, X. Sun, D. Yu, S. M. Mugo, D. Wang, Q. Zhang, *Adv. Funct. Mater.* **2023**, *33*, 2212083.
[21] X. Yang, J. Yi, T. Wang, Y. Feng, J. Wang, J. Yu, F. Zhang, Z. Jiang, Z. Lv, H. Li, T. Huang, D. Si, X. Wang, R. Cao, X. Chen, *Adv. Mater.* **2022**, *34*, 2201768.
[22] Y. Tang, S. Gan, L. Zhong, Z. Sun, L. Xu, C. Liao, K. Lin, X. Cui, D. He, Y. Ma, W. Wang, L. Niu, *Adv. Funct. Mater.* **2022**, *32*, 2107653.
[23] J. Min, J. Tu, C. Xu, H. Lukas, S. Shin, Y. Yang, S. A. Solomon, D. Mukasa, W. Gao, *Chem. Rev.* **2023**, *123*, 5049.
[24] W. Gao, S. Emaminejad, H. Y. Y. Nyein, S. Challa, K. Chen, A. Peck, H. M. Fahad, H. Ota, H. Shiraki, D. Kiriya, D. H. Lien, G. A. Brooks, R. W. Davis, A. Javey, *Nature* **2016**, *529*, 509.
[25] S. Emaminejad, W. Gao, E. Wu, Z. A. Davies, H. Yin Yin Nyein, S. Challa, S. P. Ryan, H. M. Fahad, K. Chen, Z. Shahpar, S. Talebi, C. Milla, A. Javey, R. W. Davis, *Proc. Natl. Acad. Sci. USA* **2017**, *114*, 4625.
[26] Y. Yu, J. Nassar, C. Xu, J. Min, Y. Yang, A. Dai, R. Doshi, A. Huang, Y. Song, R. Gehlhar, A. D. Ames, W. Gao, *Sci. Robot.* **2020**, *5*, eaaz7946.
[27] J. R. Sempionatto, M. Lin, L. Yin, E. De la paz, K. Pei, T. Sonsa-ard, A. N. de Loyola Silva, A. A. Khorshed, F. Zhang, N. Tostado, S. Xu, J. Wang, *Nat. Biomed. Eng.* **2021**, *5*, 737.
[28] H. Lee, T. K. Choi, Y. B. Lee, H. R. Cho, R. Ghaffari, L. Wang, H. J. Choi, T. D. Chung, N. Lu, T. Hyeon, S. H. Choi, D.-H. Kim, *Nat. Nanotech.* **2016**, *11*, 566.
[29] X. Xuan, C. Pérez-Ràfols, C. Chen, M. Cuartero, G. A. Crespo, *ACS Sens.* **2021**, *6*, 2763.

[30] H. Y. Y. Nyein, M. Bariya, B. Tran, C. H. Ahn, B. J. Brown, W. Ji, N. Davis, A. Javey, *Nat Commun* **2021**, *12*, 1823.
[31] J. R. Sempionatto, A. A. Khorshed, A. Ahmed, A. N. De Loyola e Silva, A. Barfidokht, L. Yin, K. Y. Goud, M. A. Mohamed, E. Bailey, J. May, C. Aebischer, C. Chatelle, J. Wang, *ACS Sens.* **2020**, *5*, 1804.
[32] A. J. Bandodkar, P. Gutruf, J. Choi, K. Lee, Y. Sekine, J. T. Reeder, W. J. Jeang, A. J. Aranyosi, S. P. Lee, J. B. Model, R. Ghaffari, C.-J. Su, J. P. Leshock, T. Ray, A. Verrillo, K. Thomas, V. Krishnamurthi, S. Han, J. Kim, S. Krishnan, T. Hang, J. A. Rogers, *Sci. Adv.* **2019**, *5*, eaav3294.
[33] Y. Yang, Y. Song, X. Bo, J. Min, O. S. Pak, L. Zhu, M. Wang, J. Tu, A. Kogan, H. Zhang, T. K. Hsiai, Z. Li, W. Gao, *Nat. Biotechnol.* **2020**, *38*, 217.
[34] R. M. Torrente-Rodríguez, J. Tu, Y. Yang, J. Min, M. Wang, Y. Song, Y. Yu, C. Xu, C. Ye, W. W. IsHak, W. Gao, *Matter* **2020**, *2*, 921.
[35] M. Wang, Y. Yang, J. Min, Y. Song, J. Tu, D. Mukasa, C. Ye, C. Xu, N. Heflin, J. S. McCune, T. K. Hsiai, Z. Li, W. Gao, *Nat. Biomed. Eng.* **2022**, *6*, 1225.
[36] T. R. Ray, M. Ivanovic, P. M. Curtis, D. Franklin, K. Guventurk, W. J. Jeang, J. Chafetz, H. Gaertner, G. Young, S. Rebollo, J. B. Model, S. P. Lee, J. Ciraldo, J. T. Reeder, A. Hourlier-Fargette, A. J. Bandodkar, J. Choi, A. J. Aranyosi, R. Ghaffari, S. A. McColley, S. Haymond, J. A. Rogers, *Sci. Transl. Med.* **2021**, *13*, eabd8109.
[37] X. He, T. Xu, Z. Gu, W. Gao, L.-P. Xu, T. Pan, X. Zhang, *Anal. Chem.* **2019**, *91*, 4296.
[38] X. Pei, M. Sun, J. Wang, J. Bai, X. Bo, M. Zhou, *Small* **2022**, *18*, 2205061.
[39] M. Sun, X. Pei, T. Xin, J. Liu, C. Ma, M. Cao, M. Zhou, *Anal. Chem.* **2022**, *94*, 1890.
[40] X. He, C. Fan, Y. Luo, T. Xu, X. Zhang, *npj Flex Electron* **2022**, *6*, 60.
[41] J. Tu, R. M. Torrente‐Rodríguez, M. Wang, W. Gao, *Adv. Funct. Mater.* **2020**, *30*, 1906713.
[42] O. Parlak, S. T. Keene, A. Marais, V. F. Curto, A. Salleo, *Sci Adv* **2018**, *4*, eaar2904.
[43] R. M. Torrente-Rodríguez, H. Lukas, J. Tu, J. Min, Y. Yang, C. Xu, H. B. Rossiter, W. Gao, *Matter* **2020**, *3*, 1981.
[44] B. Wang, C. Zhao, Z. Wang, K.-A. Yang, X. Cheng, W. Liu, W. Yu, S. Lin, Y. Zhao, K. M. Cheung, H. Lin, H. Hojaiji, P. S. Weiss, M. N. Stojanović, A. J. Tomiyama, A. M. Andrews, S. Emaminejad, *Sci. Adv.* **2022**, *8*, eabk0967.
[45] J. J. BelBruno, *Chem. Rev.* **2019**, *119*, 94.
[46] O. S. Ahmad, T. S. Bedwell, C. Esen, A. Garcia-Cruz, S. A. Piletsky, *Trends Biotech.* **2019**, *37*, 294.
[47] W. Tang, L. Yin, J. R. Sempionatto, J. Moon, H. Teymourian, J. Wang, *Adv. Mater.* **2021**, *33*, 2008465.
[48] J. O. Mahony, K. Nolan, M. R. Smyth, B. Mizaikoff, *Anal. Chim. Acta* **2005**, *534*, 31.
[49] J. Yao, X. Li, W. Qin, *Anal. Chim. Acta* **2008**, *610*, 282.
[50] T. Cowen, K. Karim, S. Piletsky, *Anal. Chim. Acta* **2016**, *936*, 62.
[51] M. Tabandeh, S. Ghassamipour, H. Aqababa, M. Tabatabaei, M. Hasheminejad, *J. Chromatogr. B* **2012**, *898*, 24.
[52] J. D. Fernstrom, M. H. Fernstrom, *J. Nutr.* **2007**, *137*, 1539S.
[53] R. A. Williams, C. D. S. Mamotte, J. R. Burnett, *Clin. Biochem. Rev.* **2008**, *29*, 31.
[54] N. Blau, F. J. van Spronsen, H. L. Levy, *Lancet* **2010**, *376*, 1417.
[55] J. Tirado-Rives, W. L. Jorgensen, *J. Chem. Theory Comput.* **2008**, *4*, 297.

[56] M. Azenha, P. Kathirvel, P. Nogueira, A. Fernando-Silva, *Biosens. Bioelectron.* **2008**, *23*, 1843.
[57] R. Van Deursen, P. Ertl, I. V. Tetko, G. Godin, *J. Cheminform.* **2020**, *12*, 22.
[58] R. van Deursen, P. Ertl, I. V. Tetko, G. Godin, *J. Cheminform.* **2020**, *12*, 22.
[59] T. Muhammad, Z. Nur, E. V. Piletska, O. Yimit, S. A. Piletsky, *Analyst* **2012**, *137*, 2623.
[60] M. Wang, Y. Yang, W. Gao, *Trends Chem.* **2021**, *3*, 969.